Integration of Range Split Spectrum Interferometry and Conventional InSAR to Monitor Large Gradient Surface Displacements

Haibin Luo(1,2), Zhenhong Li(2) *, Jiajun Chen(2), Christopher Pearson(2), Mingming Wang(3), Weicai Lv(4), Haiyong Ding(1)

(1) School of Remote Sensing and Geomatics Engineering, Nanjing University of Information Science and Technology, Nanjing, 210044, China.

(2) School of Engineering, Newcastle University, Newcastle upon Tyne, NE1 7RU, United Kingdom.

(3) Nanjing Kebo Space Information Technology Co., Ltd., Nanjing, 210000, China

(4) School of Geomatics, Anhui University of Science and Technology, Huainan, 232001, China)

Abstract: Incorrect unwrapping of dense interferometric fringes caused by large gradient displacements make it difficult to measure mining subsidence using conventional Interferometric Synthetic Aperture Radar (InSAR). This paper presents a Range Split Spectrum Interferometry assisted Phase Unwrapping (R-SSIaPU) method for the first time. The R-SSIaPU method takes advantage of (i) the capability of Range Split Spectrum Interferometry of measuring surface displacements with large spatial gradients, and (ii) the capability of conventional InSAR of being sensitive to surface displacements with limited spatial gradients. Both simulated and real experiments show that the R-SSIaPU method can monitor large gradient mining-induced surface movements with high precision. In the case of the Tangjiahui mine, the R-SSIaPU method agreed with GPS with differences of approximately 4.2 cm, whilst conventional InSAR deviated from GPS with differences of nearly 1 m. The R-SSIaPU method makes phase unwrapping less challenge, especially in the cases with large surface displacements. In addition to mining subsidence, it is believed that the R-SSIaPU method can be used to monitor surface displacements caused by landslides, earthquakes, volcanic eruptions, and glacier movements.

Key Words: Mining-induced Surface Displacements; Large Gradient Displacements; Range Split Spectrum Interferometry; InSAR; Phase Unwrapping

1 Introduction

Interferometric Synthetic Aperture Radar (InSAR) has been proved to be a powerful geodetic tool to monitor surface displacements caused by natural and anthropogenic processes such as earthquakes, landslides, volcanic eruptions, and mine subsidence (Cheloni et al., 2017; Cigna et al., 2014, 2017; Du et al., 2017; Simran et al., 2017; Dai et al., 2016; Tomas et al., 2014; Reinisch et al., 2017; Werner et al., 2017; Ng et al., 2017). One major limitation of InSAR is its inability to measure surface diplacements with large spatial gradients (Massonnet et al, 1998; Singleton et al., 2014).

In the region of large gradient surface diplacements caused by underground mining, unwrapping a SAR interferogram using conventional methods is difficult or even fails (Chen et al, 2001). That makes it difficult to measure large gradient surface diplacements using conventional InSAR. SAR pixel offset, also known as SAR feature tracking, was proposed to monitor large gradient surface displacements (Werner et al., 2001; Pathier et al., 2006; Yang et al., 2017). SAR pixel offset can measure large gradient surface displacements using SAR amplitude images, which has several advantages over conventional InSAR, e.g. not requiring phase unwrapping, and not being strongly limited to regions of high coherence. Note that ionosphere can impact on both phase measurements and azimuth offsets (Chen and Zebker, 2014). SAR pixel offset can measure displacement vectors in the radar line of sight (i.e. range) direction as well as the satellite flight (i.e. azimuth) direction, which are complementary to conventional InSAR since the latter only provides LOS surface displacements (Singleton et al., 2014). However, the precision of the pixel offsets depends on the pixel size of the SAR images, typically 1/20-1/30 of a pixel under the precondition of precise registration (Casu et al, 2011; Chen et al, 2015; Zhao et al., 2013). Furthermore it can only be applicable to areas with contrasting surface features (natural or man-made) and may fail in areas with limited terrain features (Singleton et al., 2014).

Range Split Spectrum Interferometry (R-SSI) applies InSAR to sub-range images obtained by splitting the available range bandwidth and explores the double differential phase through the partial interferograms to measure large gradient displacements, which cannot be measured by conventional InSAR. R-SSI has been applied successfully to measure large gradient displacements caused by earthquakes (Jiang et al, 2017) and landslides (Shi et al, 2017). Note, R-SSI has a low sensitivity to surface displacements compared with the InSAR method, as well as a high sensitivity to a pixel's signal to clutter ratio (SCR), which prevents the R-SSI method from measuring small displacements. But R-SSI has advantages over SAR pixel offset since it is less dependent on surface features. In order to monitor mining-induced surface displacements with fewer terrain features in detail, a new method, integrating R-SSI with conventional InSAR, which we denote as Range Split Spectrum Interferometry assisted Phase Unwrapping method (R-SSIaPU), is proposed. Different from the existing methods (Libert et al, 2017a, 2017b) which first unwrap conventional InSAR interferogram and then connect disconnected unwrapped patches using split spectrum interferometry, the R-SSIaPU method removes the first-order surface displacements estimated with the split spectrum interferometry, unwrap the residual interferogram and then add back the first-order displacements. The R-SSIaPU method avoids to unwrap interferograms with large gradient displacements, which makes phase unwrapping less challenge. The test shows the R-SSIaPU method can measure precisely the mining displacement in both the subsidence centre and edge.

The paper is organized as follows. In Section II, the principle of the R-SSIaPU method is presented. In Sections III and IV, the performance of the R-SSIaPU method is analysed by simulated and real experiments respectively. In Section V , conclusions are given.

2 Method

2.1 Large gradient displacements estimated using Range Split Spectrum Interferometry (R-SSI)

For any SAR image, its full range-spectrum, acquired at a centre frequency of f_0 can be split into two non-overlapping sub-bands at different carrier frequencies, f_H and f_L (indices *H* for the high sub-band and *L* for the low sub-band), using band-pass filtering (Fabio et al., 2013; Fattahi et al., 2017). A pair of SAR images (indices *M* for master and *S* for slave) at each sub-band can be used to generate two sub-band interferograms:

$$\Phi_H^W = Angle\left(I_{M,H} \cdot I_{S,H}^*\right) = -2\pi \cdot K_H - \frac{4\pi}{c} \cdot \Delta d \cdot f_H \tag{1}$$

$$\Phi_L^W = Angle\left(I_{M,L} \cdot I_{S,L}^*\right) = -2\pi \cdot K_L - \frac{4\pi}{c} \cdot \Delta d \cdot f_L \tag{2}$$

where $Angle(\cdot)$ is an operator computing the phase angles, the asterisk indicates conjugate, K is the integer cycle number, c is the velocity of light, Δd is the ground displacement between the acquisitions. So the double difference phase Φ_{Split}^{W} is given by:

$$\begin{aligned}\Phi_{Split}^{W} &= \Phi_{H}^{W} - \Phi_{L}^{W} = -2\pi \cdot \left(K_H - K_L\right) - \frac{4\pi}{c} \cdot \Delta d \cdot \left(f_H - f_L\right) \\ &= -2\pi \cdot K_{Split} - \frac{4\pi}{c} \cdot \Delta d \cdot f_{Split}\end{aligned} \tag{3}$$

If f_{split} is smaller than f_H and f_L, the interferometric fringe density of Φ_{split}^{W} is sparser than Φ_{H}^{W} and Φ_{L}^{W}. It is easier to unwrap Φ_{split}^{W} than unwrap Φ_{H}^{W} and Φ_{L}^{W}. It is important to measure large gradient displacements which often lead to too dense interference fringes to be unwrapped. Then, the displacement can be computed as follows:

$$\begin{aligned}\Delta d &= -\frac{Unwrap(\Phi_{split}^{W} + 2\pi \cdot K_{Split})}{4\pi} \cdot \frac{c}{f_{Split}} \\ &= -\frac{Unwrap(\Phi_{split}^{W})}{4\pi} \cdot \frac{c}{f_{Split}}\end{aligned} \tag{4}$$

where $Unwrap(\cdot)$ is an unwrapping operator.

Measurement uncertainty is calculated as (Bamler and Eineder, 2005):

$$\sigma_{\Delta d} = \frac{1}{4\pi} \cdot \frac{c}{f_{Split}} \cdot \sigma_{\Phi_{Split}^{W}} \tag{5}$$

where $\sigma_{\Delta d}$ and $\sigma_{\Phi_{Split}^{W}}$ are the standard deviations of Δd and Φ_{split}^{W}, respectively. $\sigma_{\Phi_{Split}^{W}}$ is given by:

$$\sigma_{\Phi_{Split}^{W}} = \sqrt{\sigma_{\Phi_{H}^{W}}^{2} + \sigma_{\Phi_{L}^{W}}^{2}} \tag{6}$$

where $\sigma_{\Phi_{H}^{W}}^{2}$ and $\sigma_{\Phi_{L}^{W}}^{2}$ are the variances of Φ_{H}^{W} and Φ_{L}^{W}, respectively. $\sigma_{\Phi_{H}^{W}}^{2}$ can be approximated by (Rodriguez et al., 1992):

$$\sigma_{\Phi_{H}^{W}}^{2} \approx \frac{1}{2N} \cdot \frac{1-\rho^2}{\rho^2} \tag{7}$$

where N is the effective number of looks and ρ is the total correlation of Φ_{H}^{W}. The variance of Φ_{L}^{W} can be also defined by Equation (7) similar to Φ_{H}^{W}.

2.2 The R-SSIaPU method

Despite the R-SSI method being able to measure the large gradient displacements, it has a lower accuracy than the InSAR method. The InSAR method can measure small displacements precisely, but it cannot measure large gradient displacements precisely due to phase unwrapping errors caused by over dense interference fringes. A concept proposed by Yun et al. (2007) is to unwrap the residual phase after a large gradient displacement phase has been subtracted from a low-frequency and low-accuracy measurement, e.g. SAR pixel offsets. Based on this concept, we proposed the Range Split Spectrum Interferometry assisted Phase Unwrapping (R-SSIaPU) method. Fig. 1 shows the workflow of the R-SSIaPU method. The R-SSI displacement is given by the R-SSI method. De Zan et al. (2015) reported that a pure late-multilooking (i.e. multilooking is done at double differential interferogram level rather than at standard interferogram level) fails to reach the theoretical performance bound of Delta-k methods, but combining the late-multilooking with some multilooking at standard interferogram level can significantly improve the efficiency. As shown in Fig 1, an adaptive filter (Goldstein and Werner, 1998) is applied to both high and low band interferograms before generating the double differential interferogram, and then a minimum cost-flow (MCF) algorithm (Costantini, 1998) is used for spatial phase unwrapping. Due to the low precision of the unwrapped double differential interferogram, a non-local filter is applied to reduce noise before converting it to surface displacements. Unlike local filters, non-local mean filtering takes a mean of all pixels in the image, weighted by how similar these pixels are to the target pixel. This results in much greater post-filtering clarity, and less loss of detail in the image compared with local algorithms (Buades et al., 2005). Then the surface displacements are converted to an initial InSAR unwrapped interferogram using the original radar wavelength. The full resolution wrapped interferogram is given by conventional InSAR processing. Then the wrapped residual interferogram is generated by complex conjugate multiplication between the full resolution InSAR wrapped interferogram and the R-SSI derived initial InSAR unwrapped interferogram. The wrapped residual interferogram is filtered and unwrapped by the MCF method. Note that the noise level of the wrapped residual interferogram is low since the InSAR wrapped interferogram is filtered at the step of the DInSAR processing and the R-SSI derived initial InSAR unwrapped interferogram is derived from the filtered unwrapped double differential interferogram. Therebefore, the adaptive filter (Goldstein and Werner, 1998) instead of non-local mean filter is used to improve the efficiency of the algorithm. The final unwrapped interferogram is obtained by adding the unwrapped residual interferogram with the R-SSI derived InSAR unwrapped interferogram. Then the final unwrapped interferogram is converted to surface displacements using the original radar wavelength.

It should be noted that the performance of the R-SSIaPU method depends on the precision of the R-SSI displacement map to some extent. If the precision is low, the R-SSIaPU might not work adequately. The precision of the R-SSI displacement map is given by the high-band interferograms phase noise, low-band interferograms phase noise and the total available range bandwidth. The lower the phase noise is, the higher the precision is. The larger the total available range bandwidth is, which gives a smaller wavelength of split spectrum (c/f_{Split}), the higher the precision is. Moreover, the performance of the R-SSIaPU method depends on the radar wavelength. If the radar wavelength is shorter, which requires higher precise initial surface displacements, the R-SSIaPU could not work adequately. Consequently, the R-SSIaPU method is more appropriate to L-band ALOS-2, which has a longer radar wavelength than X-band TerraSAR-X or C-band Sentinel-1. This is proved by the following simulated test.

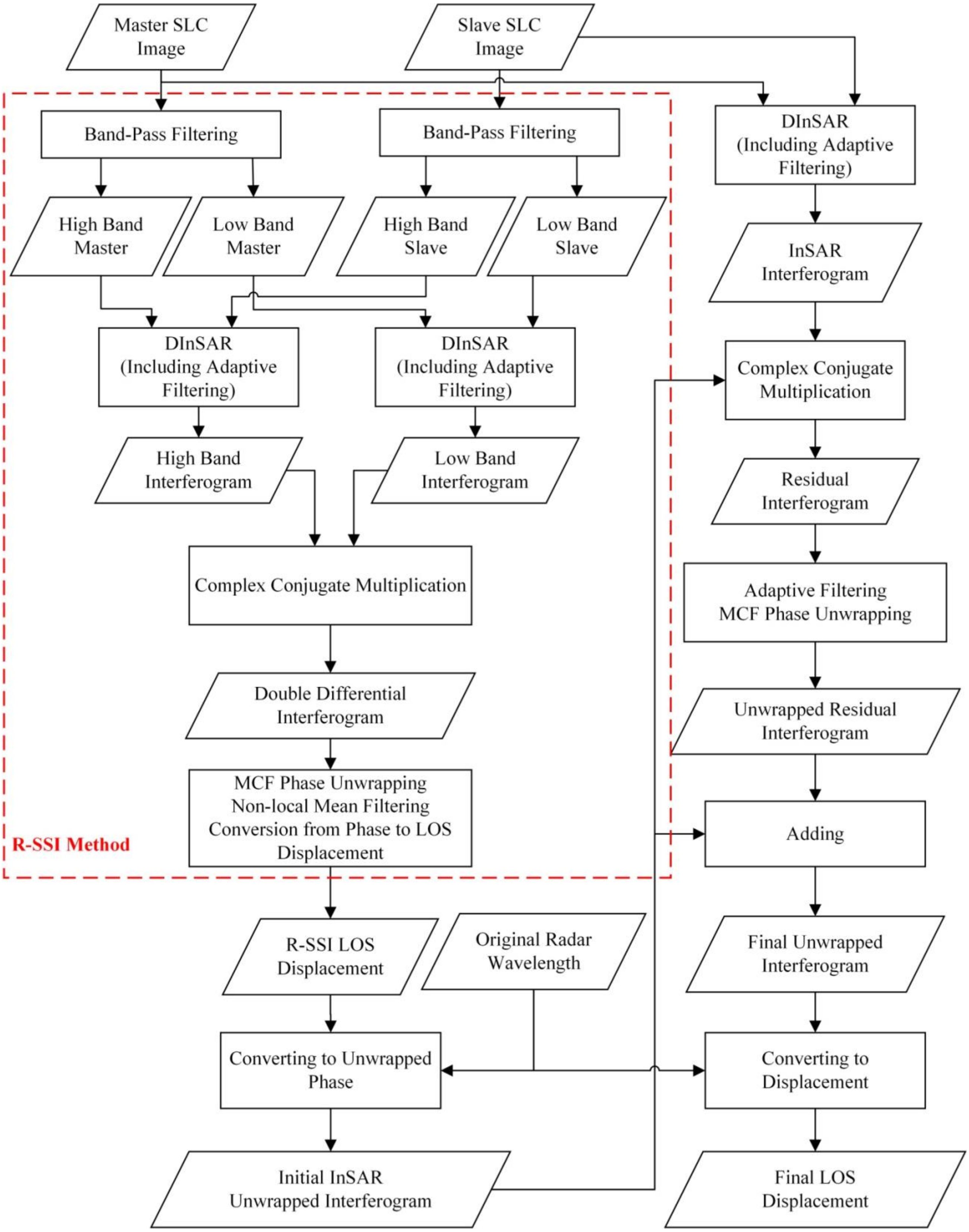

Fig. 1 The workflow of the R-SSIaPU method. Note that the workflow of the R-SSI method is indicated by the red dashed box.

3 Case Study 1: simulated mining-induced surface displacements

In order to assess the performance of the R-SSIaPU method, according to the probability integral model (Fan et al, 2014; Zhang et al, 2009), the horizontal and vertical displacements caused by coal mining are simulated on a 50×60 grid. The size of the grid point is 20×20 m. The simulated north, east and vertical displacements are shown in Fig. 2 (a), (b) and (c), respectively.

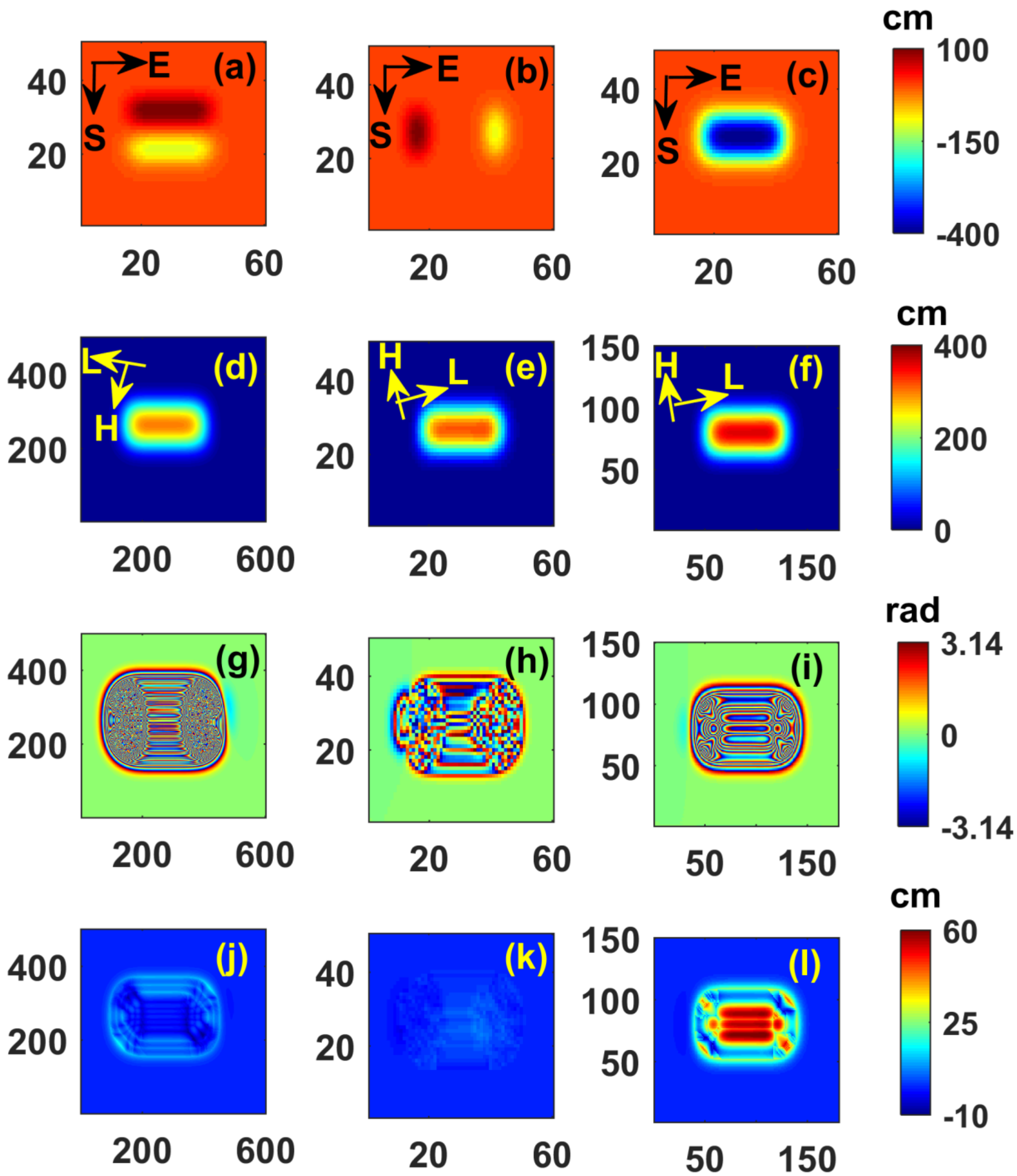

Fig. 2. Simulated mining-induced surface displacements for three different SAR sensors: (a) Northing displacements; (b) Easting displacements; (c) Vertical displacements; (d) LOS displacements for TerraSAR-X; (e) LOS displacements for Sentinel-1; (f) LOS displacements for ALOS-2; (g) wrapped interferogram for

TerraSAR-X; (h) wrapped interferogram for Sentinel-1; (i) wrapped interferogram for ALOS-2; (j) LOS displacements for TerraSAR-X derived from (g); (k) LOS displacements for Sentinel-1 derived from (h); (l) LOS displacements for ALOS-2 derived from (i).

It is clear in Fig. 2 (a) and (b) that the simulated horizontal displacements are mainly distributed at the edge of the subsidence bowl, and the displacement direction points to the centre of the subsidence bowl. The maximum displacement in the south-north direction is 110 cm, and the maximum displacement in the east-west direction is 102 cm. It is clear in Fig. 2 (c) that the centre of the subsidence bowl is dominated by vertical displacement, and the maximum displacement is 406 cm. The horizontal and vertical displacements are rescaled based on the spatial resolution listed in Table 1 and then are converted to displacements in the LOS direction (Fig 2 (d)-(f)) using Equation (8) in a matrix form.

$$d_{los} = -\left[\sin(\theta_i) \cdot \cos\left(\theta_h - \frac{3}{2}\pi\right) \quad \sin(\theta_i) \cdot \sin\left(\theta_h - \frac{3}{2}\pi\right) \quad \cos(\theta_i) \right] \cdot \left[d_{sn} \quad d_{ew} \quad d_v \right]^{\mathrm{T}} \qquad (8)$$

where d_{los} is the displacement in the LOS direction, θ_i and θ_h are the incidence angle and heading angle respectively, d_{sn}, d_{ew} and d_v are the displacements in south-north, east-west and vertical direction respectively.

The LOS surface displacements (Fig 2(d)-(f)) were converted into phase and then wrapped to generate conventional InSAR interferograms (Fig 2(g)-(i)). Obvious phase discontinuities can be observed in the subsidence trough in the simulated TerraSAR-X, Sentinel-1 and ALOS-2 interferograms (Fig 2(g)-(i)), which is entirely due to the fact that the phase gradients exceed the maximum detectable phase gradient i.e. one fringe per pixel (Massonnet and Feigl, 1998). Comparing Fig 2(j)-(l) with Fig 2(d)-(f), it is clear that conventional InSAR failed to recover the simulated mining-induced surface displacements with all the three different SAR images.

Table 1. SAR satellite characteristics relevant to simulation studies.

Bands	Satellites	Mode	Spatial resolution (m)	Heading angle (º)	Incidence angle (º)	Bandwidth (MHz)	Radar Frequency (GHz)
X	TerraSAR-X	SM	2	189.49	42.79	100	9.65
C	Sentinel-1	IWS	20	346.80	39.18	48	5.40
L	ALOS-2	SM	6.7	357.88	27.80	38	1.24

It is reported in Bamler and Eineder (2005) that the accuracy of the surface displacements estimated by the R-SSI method is maximized when the bandwidth of each sub-band is one third of the total bandwidth. Therefore, a band-pass filtering was employed to split the range bandwidth listed in Table 1 to form the sub-bands at ±B/3 (B is range bandwidth) from the radar frequencies with the sub-band bandwidth of B/3 (Furuya et al., 2017). This band-pass filtering was done before the co-registration of the SLCs to avoid the impacts of spectral shifts at the step of the resampling of the slave SLC image. The sub-band SLCs were demodulated to shift the spectrum to the center of the sampled spectrum with a phase ramp and to change the center frequencies to the new values. Using the centric frequencies of each sub-bands, the LOS displacements are transformed into phases and then wrapped into wrapped interferograms. Gaussian noise of a form $N = (0, \sigma = 10°)$ was added to each simulated sub-band wrapped interferogram. Then, the simulated high band, low band and conventional InSAR wrapped interferograms are processed as the workflow presented in Fig. 1. The residual errors are presented in Fig. 3 and the RMS statistics are listed in Table 2.

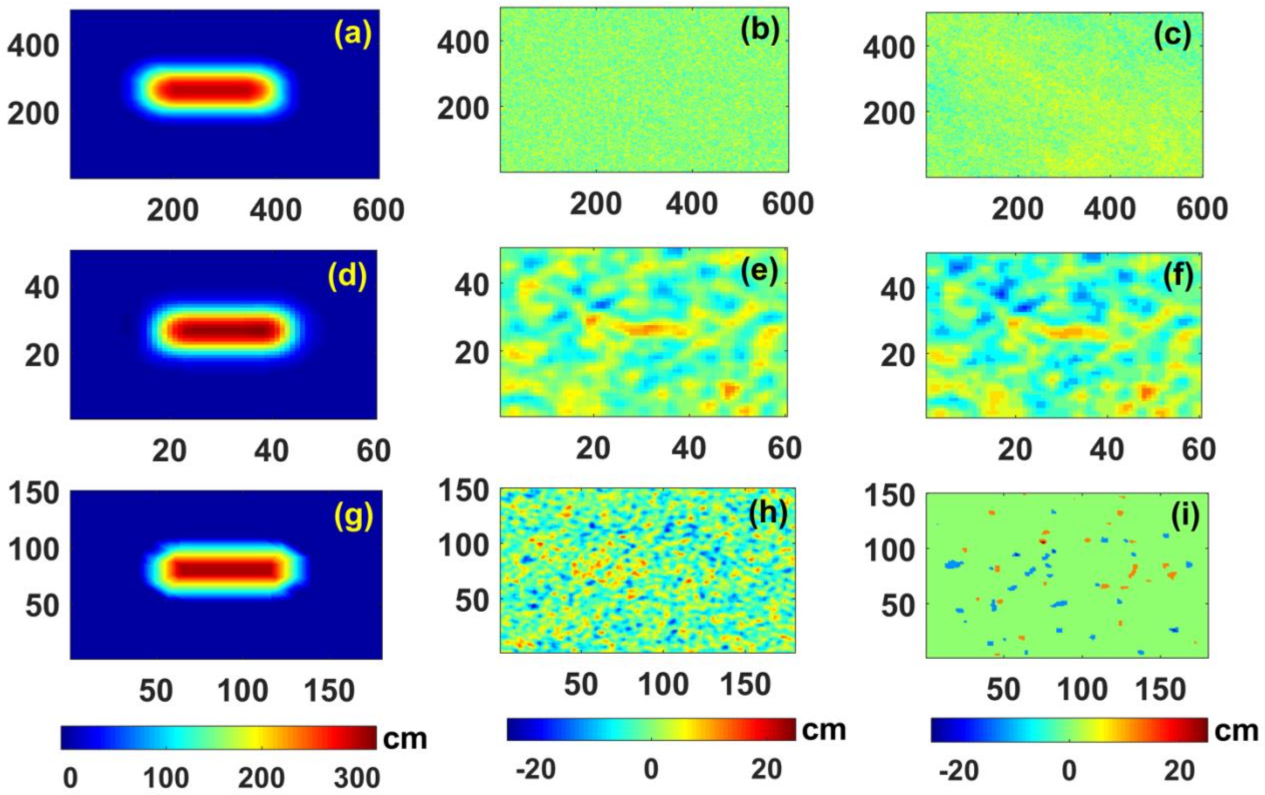

Fig. 3. Residuals between the simulated and calculated LOS displacements: (a)-(c) are derived from conventional InSAR, the R-SSI method and the R-SSIaPU method for TerraSAR-X; (d)-(f) are the same as (a)-(c), but for Sentinel-1; (g)-(i) are the same as (a)-(c), but for ALOS-2.

Table 2. Maximum detectable displacements over a distance of 100 m and the corresponding RMS statistics for different approaches

Satellites	$d_{max,LOS}$ of InSAR[(a)] (m)	$d_{max,LOS}$ of R-SSI (m)	Radar wavelength (m)	Wavelength of R-SSI[(b)] (m)	Accuracy of InSAR displacements (mm)	Accuracy of R-SSI displacements (mm)	Accuracy of R-SSIaPU displacements (mm)
TerraSAR-X	0.388	56.213	0.031	4.497	743.8	19.4	24.1
Sentinel-1	0.070	11.638	0.056	9.310	784.5	40.1	47.3
ALOS-2	0.896	44.157	0.240	11.834	764.9	52.5	21.1

(a) $d_{max,LOS}$ is the maximum detectable displacement in the LOS direction which is given by $d_{max,LOS} \approx \frac{w}{g_{resolution}} \cdot \frac{\lambda}{4}$, where, $g_{resolution}$ is the pixel resolution and w (100 m in this paper) is the radius of the subsidence bowl, λ is the wavelength (Ng et al., 2017). (b) Wavelength of R-SSI= c/f_{Split} .

It can be seen that for all the three satellites, the conventional InSAR method gives large residual errors (Fig. 3 (a), (d) and (g)) in the centre of the subsidence bowl, where phase unwrapping errors occur due to the dense fringes caused by the large gradient displacements which exceed the maximum detectable phase gradients of conventional InSAR i.e. one fringe per pixel (Massonnet and Feigl, 1998). The residual errors (Fig. 3 (b), (e) and (h)), derived from the R-SSI method are small. The smallest R-SSI RMS is given by the TSX-1 satellite since it has the smallest wavelength of R-SSI while the same noise level as that of Sentinel-1 and ALOS-2 (see equation 5). For the TSX-1 and S1-A satellites the R-SSIaPU method cannot improve the accuracies (Fig. 3 (c) and (f)). This is because the shorter wavelength (3.1 cm for TSX-1 and 5.6 cm for S1-A) requires higher sensitivity to the displacement gradient provided by the R-SSI method. For the ALOS-2 pair, a significant improvement can be seen in most areas and the improvement ratio of RMS is 59.7%. However, there are large residuals (Fig. 3 (i)) in some small areas resulting from the uncertainties in the R-SSI derived surface displacements. These residuals are an integer multiple of half of the radar wavelength and may be corrected manually in some cases.

4 Case Study 2: Subsidence at the Tangjiahui coal mine, China

The study area is located in the Tangjiahui coal mining area in the Inner Mongolia autonomous region, China (Fig. 4). The TangJiahui coal mine is located in the northeastern margin of the Ordos syncline in the North China platform. The basic structure is a monoclinic structure with undulating waves and a near north-south strike. The northern strata strike of the structure is nearly the east-west whilst its southern strata strike changes to the northwest. The outline of the structure likes an ear. The dip angle at the edge of the basin is slightly larger and a short back syncline whose axial direction is approximately parallel to the edge of the basin exists. The dip in the basin is small, usually below 10 degrees, and there is a sublevel fold which is perpendicular to the strata strike. The sublevel fold is generally small and has little extension, resulting in the relative fluctuation of the seam floor contour. Fractures in the coalfield are not developed, and only a few small tensile faults exist. In the TangJiahui coal mine, the elevation at the north is greater than that at the south. The highest point is located in the northeast of the well field and the lowest point located in the south of the well field. The maximum elevation difference is 195.57 m and the average elevation is 1220-1300 m. As part of the Ordos Plateau, the area is covered by quaternary loess with ravines and gullies. Coal mining began in December 2015, and the mining direction is from southeast to northwest (Fig 4(a)). The mine face has a length of 962 m, a width of 230m, and a depth of approximately 521 m. The overlying bedrock is mainly composed of detrital sedimentary rocks with layered structure, the mechanical strength of rock is low, and the stability is poor. Therefore, coal mining activities can easily result in the collapse of mined voids and then large subsidence.

We used the ascending ALOS-2 pair of 25 December 2015 and 4 March 2016, path 140, frame 790, both acquired in the sm2 operation mode. The perpendicular baseline is 44 m. Two GPS stations were located along the mining direction to monitor surface displacements. During the period from 25 December 2015 to 4 March 2016, the northing, easting and vertical displacements measured by GPS were -0.0279 m, 0.0178 m and -0.0150 m at Station #1 and -0.2029 m, 0.3399 m and -0.9941m at Station #2. The LOS displacements converted from the three dimensional displacements at Stations #1 and #2 are -0.0190 m and -1.0115 m, respectively. The large displacement at GPS Station #2 makes it difficult to monitor the displacements with the conventional InSAR method.

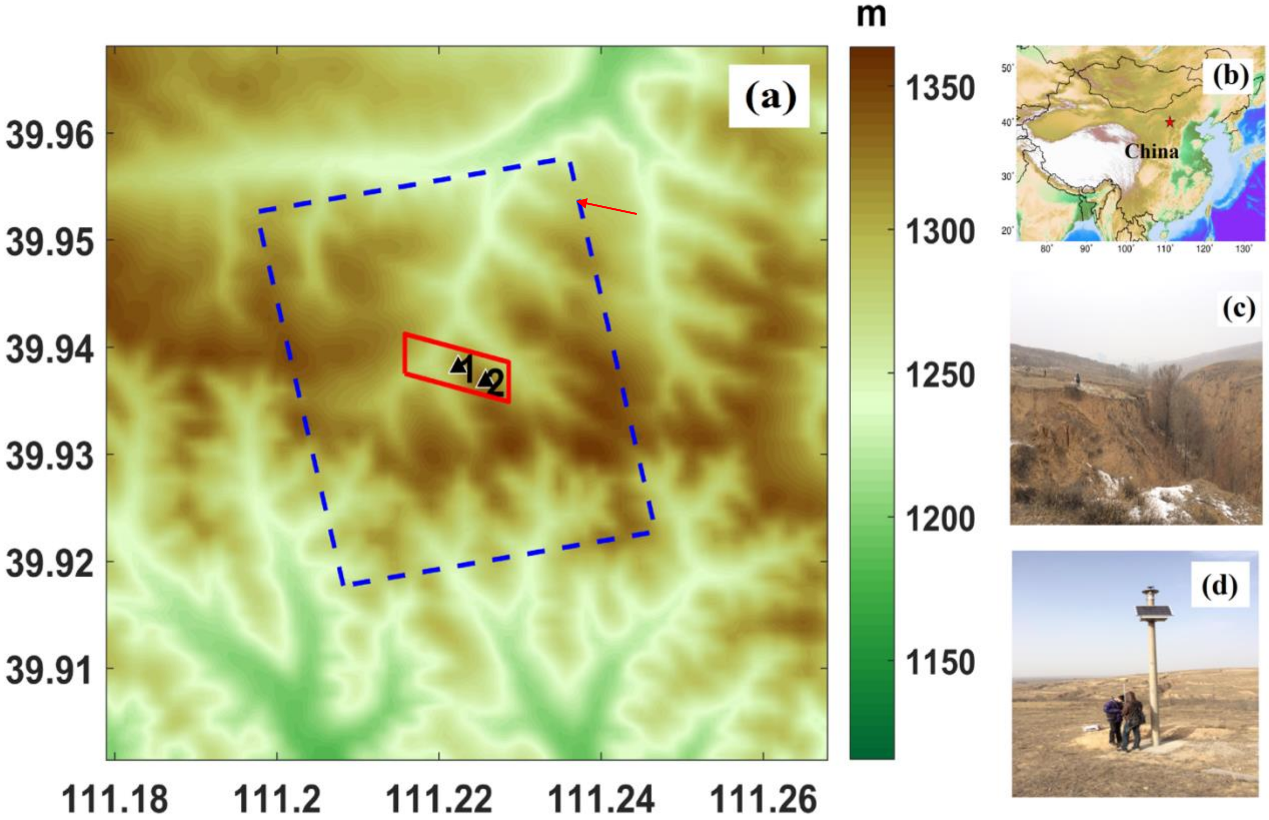

Fig. 4 Case Study 2: (a) The mine face and GPS stations overlaid on SRTM DEM. Note that (i) the mine face is indicated by the red solid rectangle; (ii) the mining direction is implied by the red arrow; and (iii) the blue dashed box represents the coverage of ALOS-2 images. (b) Location of the study area in a China map; (c) A photo showing the overall mine face; (d) A photo of GPS Station #1.

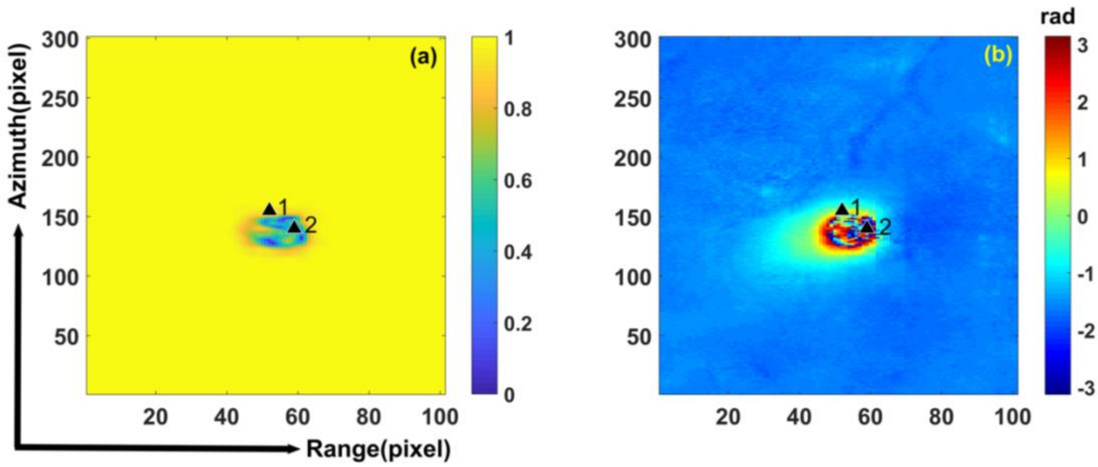

Fig. 5 Case Study 2: (a) ALOS-2 coherence map; (b) ALOS-2 wrapped interferogram (unit: radians)

Fig. 5 shows the ALOS-2 coherence map as well as the wrapped interferogram. It is clear in Fig 5(a)-(b) that coherence is generally high except for the deforming area with dense fringes (e.g. GPS Stations #2 and its surrounding area), which makes phase unwrapping a big challenge for conventional InSAR.

As mentioned in the simulated analysis, we split the range bandwidth using a band pass filter to form the sub-bands at ±B/3 (B is the range bandwidth) from the radar frequencies with the sub-band bandwidth of B/3. Then the filtered data are processed as seen in the workflow presented in Fig. 1. The results are shown in Fig. 6. The result given by the conventional InSAR is presented together for comparison.

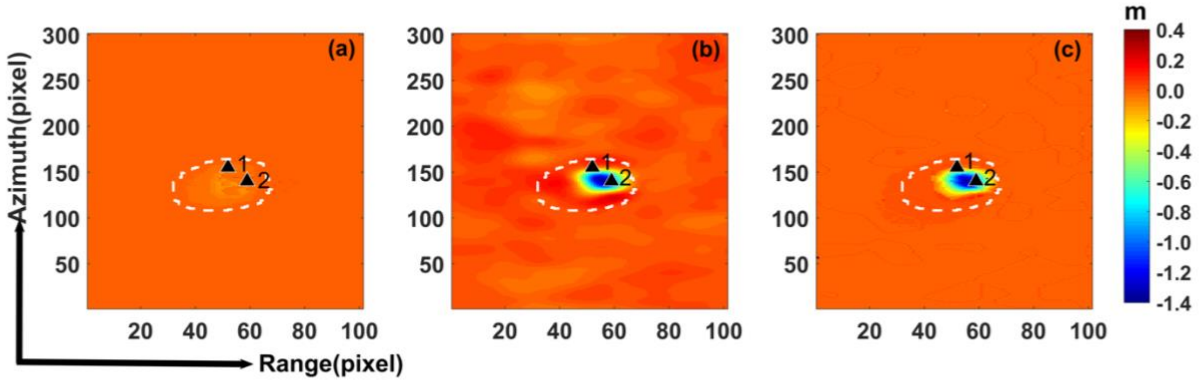

Fig. 6 LOS surface displacements derived from (a) conventional InSAR, (b) R-SSI, and (c) R-SSIaPU. The white dashed line represents the rough boundries of the deforming area.

Conventional InSAR can measure small surface displacements with higher precision than R-SSI, which can be evidenced by the smoother signals in the far field (i.e. those outside the white ellipse) in Fig 6(a) than those in Fig 6(b). However, due to the incorrect unwrapping in the subsidence centre, its maximum displacement is only about -0.133 m , which deviated significantly from the magnitude of the surface displacements measured by GPS. The R-SSI method measures a larger displacement, -1.3749 m, in the subsidence centre. The R-SSIaPU method (Fig. 6(c)) integrates the advantages of the two methods above, suggesting a similar displacement shape to conventional InSAR and gives the max displacement of -1.3624 m, which is approximately equal to that of the R-SSI method.

Table 3. The maximum LOS displacements, residuals and RMS given by conventional InSAR, the R-SSI method and the R-SSIaPU method.

Methods	Max LOS displacements (m)	Difference with GPS (m)		Displacement RMS in non-deforming area (m)
		Station 1 (-0.0190[a])	Station 2 (-1.0115[a])	
InSAR	-0.133	0.019	-0.979	0.002
R-SSI	-1.375	0.047	0.073	0.036
R-SSIaPU	-1.362	0.039	0.042	0.006

(a) The surface displacements measured by GPS

Table 3 lists the residual displacements of three methods at GPS Stations #1 and #2. At GPS Station #1 which has a small displacement, conventional InSAR gives the minimum residual due to its high precision. The R-SSI method gives a maximum residual due to its large wavelength and interferometric phase noise which is approximately $\sqrt{2}$ times that of InSAR. The R-SSIaPU method improves the results of the R-SSI method and gives smaller residual. At GPS Station #2 which has a large displacement, conventional InSAR gives the maximum residual due to the error in phase unwrapping. The R-SSI method gives the smaller residual and the R-SSIaPU gives the minimum residual. In order to measure the precision of the three methods, the non-deforming area, whose displacements given by InSAR are smaller than 0.02 m, are separated. Assuming a zero displacement in the non-deforming area, we can compute the RMS of the non-deforming area for each method.

The InSAR method gives the minimum RMS and the R-SSIaPU method improved R-SSI RMS from 0.036 m to 0.006 m. The real data analysis fully proves that the R-SSIaPU method has a higher accuracy than the R-SSI method.

5 Discussion and conclusions

Large gradient displacements of the Earth's surface caused by natural hazards and utilization of natural resources have been observed in many places. Examples include the following: earthquakes (e.g. Pathier et al., 2006); landslides (e.g. Singleton et al., 2014), volcanos (e.g. Yun et al., 2007), exploitation of groundwater (e.g., Chen et al., 2016; Liu et al., 2016), and coals (e.g. Yan et al., 2016; Yang et al., 2017). All of these can cause damages to buildings or infrastructure, and loss of life and injury to citizens. Hence it is crucial to detect and monitor large gradient displacements. The R-SSIaPU method has been presented in this paper by integrating Range Split Spectrum Interferometry and conventional InSAR to monitor large gradient surface displacements with high precision. The proposed method unwraps the InSAR residual phase after a complex and large gradient displacement phase (initial unwrapped phase) is subtracted from a low-precision displacement map derived from the Range Split Spectrum Interferometry method. Then the final displacement map is generated by converting the total unwrapped phase (residual unwrapped phase + initial unwrapped phase) to LOS surface displacements with the original radar wavelength. The proposed R-SSIaPU method has been applied to investigate the surface displacements caused by mining activities in Tangjiahui, and a good agreement is observed with GPS measurements. It is also found from the simulated test that the total range bandwidth and the original radar wavelength are the two controlling factors of the performance of the R-SSIaPU method. The greater the range bandwidth and the radar wavelength, the better the R-SSIaPU method performs.

The R-SSIaPU method is easy to implement using conventional InSAR software, and can be applicable to areas with few characteristic objects where SAR pixel offset may fail, for example the Tangjiahui mine presented in the real data analysis. The R-SSIaPU method has inherent advantages over the SAR pixel offset based phase unwrapping as demonstrated in Yun et al (2007): (i) R-SSI is less sensitive to the pixel size of the SAR images than SAR pixel offset, and (ii) the former is much faster in terms of computational efficiency. However, it should be noted that the performance of the R-SSIaPU method is also dependent upon the coherence of the SAR images, which limits its application to a densely vegetated region where rapid decorrelation happens between SAR acquisitions. Nevertheless, the results showed that the R-SSIaPU method makes phase unwrapping less challenge, especially in the cases with large surface displacements.

Acknowledgment

This research was supported by Natural Science Foundation of China (No. 41301400, 41571350, and 41474026). This work was also partially supported by the UK NERC through the Centre for the Observation and Modelling of Earthquakes, Volcanoes and Tectonics (COMET, ref.: come30001) and the LICS and CEDRRIC projects (ref. NE/K010794/1 and NE/N012151/1, respectively), and the ESA-MOST DRAGON-4 project (ref. 32244). The authors would like to thank Dr. Bingqian Chen for providing simulated coal mining data and useful discussions.

References

Bamler, R., Eineder, M., 2005. Accuracy of differential shift estimation by correlation and split-bandwidth interferometry for wideband and delta-k SAR systems. IEEE Geoscience and Remote Sensing Letters, 2(2):151-155.

Buades, A., Coll, B., Morel J., 2005. A non-local algorithm for image denoising. 2005 IEEE Computer Society

Conference on Computer Vision and Pattern Recognition (CVPR'05).

Casu, F., Manconi, A., Pepe, A., Lanari, R., 2011. Deformation time-series generation in areas characterized by large displacement dynamics: the SAR amplitude pixel offset SBAS technique. IEEE Transaction on Geoscience and Remote Sensing, 49:2752–2763.

Cheloni, D., Novellis, V., Albano, M., Antonioli, A., Anzidei, M., Atzori, S., Avallone, A., Bignami, C., Bonano, M., Calcaterra, S., Castaldo, R. Casu, F., Cecere, G., Luca, C., Devoti, R., Bucci, D., Esposito, A., Galvani, A., Gambino, P., Giuliani, R., Lanari, R., Manunta, M., Manzo, M., Mattone, M., Montuori, A., Pepe, A., Pepe, S., Pezzo, G., Pietrantonio, G., Polcari, M., Riguzzi, F., Salvi, S. Sepe, V., Serpelloni, E., Solaro, G., Stramondo, S., Tizzani, P., Tolomei, C., Trasatti, E., Valerio, E., Zinno, I., Doglioni, C., 2017. Geodetic model of the 2016 Central Italy earthquake sequence inferred from InSAR and GPS data. Geophysical Research Letters, 44, 6778–6787.

Chen, B., Deng, K., Fan, H., Yu, Y., 2015. Combining SAR interferometric phase and intensity information for monitoring of large gradient deformation in coal mining area. European Journal of Remote Sensing, 48(1):701-717.

Chen, M., Tomás, R., Li, Z., Motagh, M., Li, T., Hu, L., Gong, H., Li, X., Yu, J., Gong, X., 2016. Imaging land subsidence induced by groundwater extraction in Beijing (China) using satellite radar interferometry. Remote Sensing, 8(6), 468.

Chen, C., Zebker, H., 2001. Two-dimensional phase unwrapping with use of statistical models for cost functions in nonlinear optimization. Journal of the Optical Society of America A-Optics Image Science and Vision, 18:338–351.

Chen, A. C., Zebker, H., 2014. Reducing ionospheric effects in InSAR data using accurate coregistration. IEEE Transactions on Geoscience and Remote Sensing, 52(1), 60-70.

Cigna, F., Banks, J.V., Donald, W.A., Donohue, S., Graham, C., Hughes, D., McKinley, M.J., Parker, K., 2017. Mapping ground instability in areas of geotechnical infrastructure using satellite InSAR and small UAV surveying: a case study in Northern Ireland. Geosciences 7.

Cigna, F., Lasaponara, R., Masini, N., Milillo, P., Tapete, D., 2014. Persistent scatterer interferometry processing of COSMO-SkyMed stripmap HIMAGE time series to depict deformation of the Historic Centre of Rome, Italy. Remote Sensing 6.

Costantini, M., 1998. A novel phase unwrapping method based on network programming. IEEE Transactions on Geoscience and Remote Sensing, 36(3), 813-821.

Dai, K., Li, Z., Tomás, R., Liu, G., Yu, B., Wang, X., Cheng, H., Chen, J., Stockamp, J., 2016. Monitoring activity at the Daguangbao mega-landslide (China) using Sentinel-1 TOPS time series interferometry. Remote Sensing of Environment, 186:501-513.

De Zan, F., Prats-Iraola, P., Rodriguez-Cassola, M., 2015. On the Dependence of delta-k efficiency on multilooking. IEEE Geoscience and Remote Sensing Letters, 12(8), 1745-1749.

Du, Y., Xu, Q., Zhang, L., Feng, G., Li, Z., Chen, R.-F., Lin, C.-W., 2017. Recent landslide movement in Tsaoling, Taiwan Tracked by TerraSAR-X/TanDEM-X DEM time series. Remote Sensing, 9.

Fan, H., Gu, W., Qin, Y., Xue, J., Chen, B., 2014. A model for extracting large deformation mining subsidence using D-InSAR technique and probability integral method. Transactions of Nonferrous Metals Society of China, 24(4):1242-1247.

Fabio, B., Giacovazzo, V., Refice, A., Veneziani, N., 2013 .Multichromatic analysis of InSAR data. IEEE Transactions on Geoscience and Remote Sensing, 51(9):4790-4799.

Fattahi, H., Simons, M., Agram, P., 2017. InSAR time-series estimation of the ionospheric phase delay: an extension of the split range-spectrum technique. IEEE Transactions on Geoscience and Remote Sensing, 55(10): 5984- 5996.

Goldstein, R. M., Werner, C. L., 1998. Radar interferogram filtering for geophysical applications. Geophysical

Research Letters, 25(21), 4035-4038.

Furuya, M., Suzuki, T., Maeda, J., Heki, K., 2017. Midlatitude sporadic-E episodes viewed by L-band split-spectrum InSAR, Earth, Planets and Space, 69(1), 175.

Jiang, H., Feng, G., Wang, T., Bürgmann, R., 2017. Toward full exploitation of coherent and incoherent information in Sentinel-1 TOPS data for retrieving surface displacement: application to the 2016 Kumamoto (Japan) earthquake. Geophysical Research Letters, 44, 1758–1767, doi:10.1002/2016GL072253.

Libert, L., Derauw, D., d'Oreye, N., Barbier, C., Orban, A., 2017a. Split-band interferometry-assisted phase unwrapping for the phase ambiguities correction. Remote Sensing, 9.

Libert, L., Derauw D., Barbier C., 2017b. Optimum split-band parameters for phase offset retrieval. Geoscience and Remote Sensing Symposium (IGARSS), doi:10.1109/IGARSS.2017.8126900.

Liu, P., Li, Q., Li, Z., Hoey, T., Liu, G., Wang, C., Hu, Z., Zhou, Z., Singleton, A., 2016. Anatomy of subsidence in Tianjin from time series InSAR. Remote Sensing, 8(3).

Massonnet, D., Feigl, K., 1998. Radar interferometry and its application to changes in the Earth's surface. Reviews of Geophysics, 36(4), 441-500.

Ng, A., Ge, L., Du, Z., Wang, S., Ma, C., 2017. Satellite radar interferometry for monitoring subsidence induced by longwall mining activity using Radarsat-2, Sentinel-1 and ALOS-2 data. International Journal of Applied Earth Observation and Geoinformation. 61:92-103.

Pathier, E., Fielding, E., Wright, T., Walker, R., Parsons, B., Hensley, S., 2006. Displacement field and slip distribution of the 2005 Kashmir earthquake from SAR imagery. Geophysical Research Letters, 33, L20310, doi:10.1029/2006GL027193.

Reinisch, E., Cardiff, M., Feigl, K., 2017. Graph theory for analyzing pair-wise data: application to geophysical model parameters estimated from interferometric synthetic aperture radar data at Okmok volcano, Alaska. Journal of Geodesy, 91(1):9-24.

Rodriguez, E., Martin, J., 1992. Theory and design of interferometric synthetic aperture radars. IEE Proc. Part F Radar Signal Process, 139(2):149–159.

Shi, X., Jiang, H., Zhang, L., Liao, M., 2017. Landslide displacement monitoring with split-bandwidth interferometry: a case study of the shuping landslide in the Three Gorges Area. Remote Sensing, 9, 937; doi:10.3390/rs9090937.

Simran, S., Peltzer, G., Zhang, A., Meng, L., Liang, C., Lundgren, P., Fielding, E., 2017. Fault geometry of 2015, Mw7.2 Murghab, Tajikistan earthquake controls rupture propagation: Insights from InSAR and seismological data. Earth and Planetary Science Letters, 462: 132-141.

Singleton, A., Li, Z., Hoey, T., Muller, J., 2014. Evaluating sub-pixel offset techniques as an alternative to D-InSAR for monitoring episodic landslide movements in vegetated terrain. Remote Sensing of Environment, 147:133-144,

Tomas, R., Li, Z., Liu, P., Singleton, A., Hoey, T., Cheng, X., 2014. Spatiotemporal characteristics of the Huangtupo landslide in the Three Gorges region (China) constrained by radar interferometry. Geophysical Journal International, 197:213–232.

Werner, C., Strozzi, T., Wiesmann, A., Wegmuller, U., Murray, T., Pritchard, H., Luckman, A., 2001. Complimentary measurement of geophysical deformation using repeat-pass SAR. IEEE International Geoscience and Remote Sensing Symposium, 9-13 July 2001, Sydney, pp. 3255-3258.

Werner, W., Freysteinn, S., Stéphanie, D., Lavallée, Y., 2017. Post-emplacement cooling and contraction of lava flows: InSAR observations and a thermal model for lava fields at Hekla volcano, Iceland. Journal of Geophysical Research: Solid Earth, 122(2):946–965.

Yan, S., Liu, G., Deng, K., Wang, Y., Zhang, S., Zhao, F., 2016. Large deformation monitoring over a coal mining region using pixel-tracking method with high-resolution Radarsat-2 imagery, Remote Sensing

Letters, 7(3), 219-228.
Yang, Z., Li, Z., Zhu, J., Preusse, A., Yi, H., Hu, J., Feng, G., Papst, M., 2017. Retrieving 3-D large displacements of mining areas from a single amplitude pair of SAR using offset tracking. Remote Sensing, 9(4).
Yun, S., Zebker, H., Segall, P., Hooper, A., Poland, M., 2007. Interferogram formation in the presence of complex and large deformation. Geophysical Research Letters, 34, L12305, doi:10.1029/2007GL029745.
Zhang, H., Wang, Y., Li, Y., 2009. SVM model for estimating the parameters of the probability-integral method of predicting mining subsidence. Mining Science and Technology (China), 19(3):385-388.
Zhao, C., Lu, Z., Zhang, Q., 2013. Time-series deformation monitoring over mining regions with SAR intensity-based offset measurements. Remote Sensing Letters, 4:436-445.